



Evaluating failure regime of an active landslide using instability and rockfall simulation, NW Himalaya

Imlirena Jamir^{1,6} · Vipin Kumar² · Arun Kumar Ojha^{1,6} · Vikram Gupta³ · Tapas Ranjan Martha⁴ · D. V. Griffiths⁵

Received: 30 July 2023 / Accepted: 4 March 2024 / Published online: 12 April 2024
© The Author(s), under exclusive licence to Springer-Verlag GmbH Germany, part of Springer Nature 2024

Abstract

The NW Himalaya has been subjected to frequent disastrous landslides of different types owing to frequent extreme rainfall events and rock mass shearing caused by structural and/or lithological contrast. Though majority of the landslides in the NW Himalaya are of complex type comprising debris and loose rock mass that may result into debris flow and/or rockfall, their potential behavior is rarely explored. The present study aims to evaluate the recurrence of one such complex landslide (0.23 Mm²) of Yamuna Valley, NW Himalaya that is subjected to rock mass shearing and the region accommodating this landslide receives frequent extreme rainfall events. A huge slope failure in this landslide occurred on 12 September, 2017 damaging a ~400 m stretches of the National Highway (NH) road. The landslide location has strategic significance, since up to 0.3–0.4 million pilgrims travel annually on the road passing through the landslide slope. To evaluate the potential behavior of landslide and to understand the factors causing this landslide (pre-failure analysis), slope stability analysis and rockfall simulation were performed. Pre-failure analyses indicated that the maximum shear strain of 0.14–0.18 and total displacement of 2–8 m likely developed parallel to the slope. The possibility of rainfall triggering is explored in view of increasing rainfall, soil moisture, and surface runoff conditions. Tectonic influences are also evaluated using joints and fracture patterns in rock mass. Post-failure analysis showed that though the maximum shear strain and the total displacement had reduced to 0.07–0.15 and 2–5 m, respectively after the failure, the slope is still unstable. Rockfall simulation revealed the potential for rockfalls having energy and velocities in the range of 900–4000 kJ and 18–75 m/s, respectively.

Keywords Landslide · Slope stability · Rockfall · Climate · Himalaya · Yamuna valley

Introduction

The most likely threats for the community living in the hills are increased frequency and magnitude of landslides and floods (Märgärnt et al. 2013; Bălteanu et al. 2020; Gong et al. 2021; Kumar et al. 2019; Sundriyal et al. 2023a,

b). Tectonic activity and its associated structures such as foliations, faults, folds, joints and cleavages, along with precipitation, can greatly influence the spatial distribution and frequency of landslides in a region (Keefer et al. 1984; Alexander and Formichi 1993; Gorum 2019; Cui et al. 2018; Jamir et al. 2020; Qi et al. 2021). Further, in such tectonic settings, large landslides can take many forms, including slow-moving creep failure, rapid debris flow and rockfall due to intensive shearing, resulting in localized deterioration of rock strength (Krautblatter and Moser 2009; Morelli et al. 2010; Melillo et al. 2020). Among the different forms of mass movements, shallow landslides are quite common and mostly impact superficial deposits influenced by deformation of soil or weathered rocks (Leroueil et al. 1996; Wang et al. 2019). Such mass movements are often attributed to intense and/or sustained rainfall events, which reduce the shear strength of the soil and hence the stability of the slope. As such, investigation of slope morphology, overburden on the slope and rock properties, plays a crucial

✉ D. V. Griffiths
vgriffit@mines.edu

¹ CSIR-National Geophysical Research Institute, Hyderabad, India

² Department of Geology, Nityanand Himalayan Research and Study Centre, Doon University, Dehradun, India

³ Department of Geology, Sikkim University, Sikkim, India

⁴ National Remote Sensing Centre, Hyderabad, India

⁵ Colorado School of Mines, Golden, USA

⁶ Academy of Scientific and Innovative Research (AcSIR), Ghaziabad, India

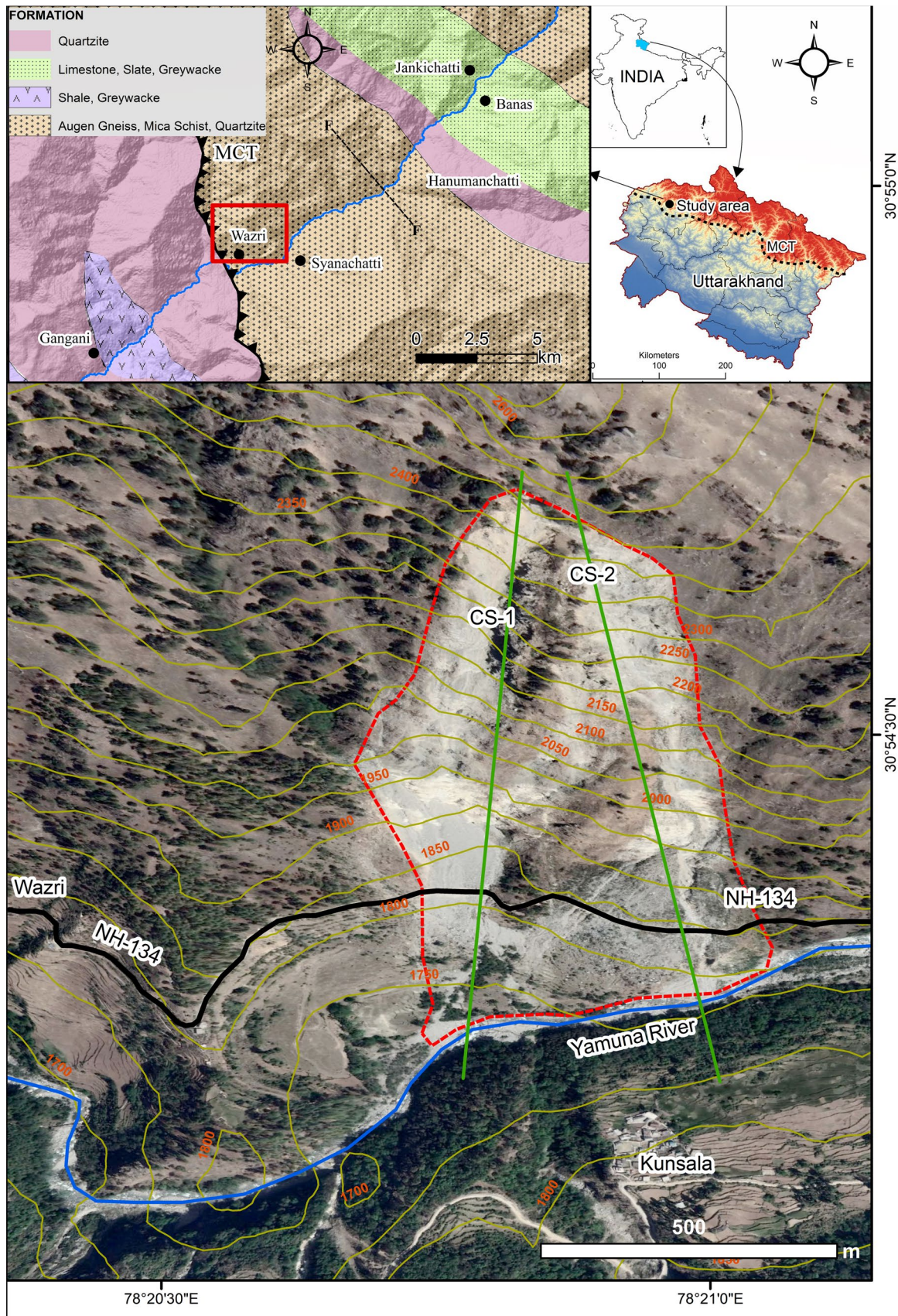


Fig. 1 Location map of the study area. Inset geological map is based on Jamir et al. (2020). Contour lines are extracted from Cartosat 1 DEM. The CS-1 and CS-2 indicate the cross-sections taken for slope stability analysis (“Slope stability”)

role in understanding the potential failure mechanisms of a landslide. Hence, the need, to understand the extent of an unstable area and the potential risk to the ecosystem should a landslide occur, has become a major task containing many uncertainties.

Despite the fact the NW Himalaya in India has been subjected to frequent landslides in last decades, studies evaluating the potential impact of active landslides and their recurrence potential have been relatively rare. At present, several continuum/dis-continuum numerical simulations can be adopted to understand such recurrence potential of landslides (Griffiths and Lane 1999; Jing 2003; Eberhardt et al. 2004; Jamir et al. 2017; Kumar et al. 2021a, b; Shaller et al. 2020; Zheng et al. 2021). Notably, different numerical approaches can be used to ascertain the probability of failure (or factor of safety) of slopes pre-failure, and the post-failure behavior including estimates of run-out distances (Cascini et al. 2009; Setiawan et al. 2019; Wei et al. 2019; Zheng et al. 2021). Specific to the Himalaya, though there have been various studies to better understand the triggering of landslides (Gupta et al. 2017; Jamir et al. 2017; Jamir et al. 2020, Kumar et al. 2021b; Roy et al. 2022), a gap related to investigations for early indications of slope instability still exists.

Therefore, to fill such a gap in the NW Himalayan terrain an attempt is made by performing a case study. The case study involves a complex landslide (0.23 Mm² total disturbed area) that occurred as a rockfall on 12 September 2017 due to antecedent rainfall, followed by a series of events on the 22–23 September, 2017 near Wazri (or Ojari) village in the Yamuna Valley, NW Himalaya, India. During these events, it completely damaged 400-m long stretch of the National Highway (NH-134), affected socio-economic activities of 12 villages in the area, and also required the national authorities to invest ~US\$0.9 M for the safe passage along this route (IANS 2019a). Further, this landslide has developed a tendency to be more active in the form of debris slide and/or flow during the months of June–September (Indian Summer Monsoon months), which is also the season of the “Char Dham (shrine) Pilgrimage” along this route (Haberman 2006; Karar 2010). Notably, up to 0.42 million pilgrims were estimated to have visited the Yamunotri shrine, within the region of this study, between May and September, 2022. The potential for serious life-threatening consequences of this landslide makes it imperative to evaluate the possible recurrence of further failure by investigating 2D continuum modeling-based slope stability, potential rockfall simulation scenarios, structural mapping, and

precipitation regimes. Though ideal recurrence evaluation should also involve subsurface imaging of the hillslope enabling 3D back analysis, limitations subjected to steep terrain accessibility and economic resources make 2D evaluation of this study rationally viable. Findings and concept of this case study can be replicated in those regions of mountains, which involve human habitation and sheared rock mass hillslope in the proximity.

Study area

The landslide is located at 78°20′ 49.92′ E and 30°54′ 21.03′ N along the National Highway (NH-134), near Wazri village (or Ozari/ Bazari) in the Yamuna Valley, NW Himalaya, India (Fig. 1). The landslide is on the right bank of the Yamuna River, which is a perennial river that originates from the Saptrishi Kund (lake) situated at an altitude of 4200 m, which in turn is fed by the Bander Punch glacier (6315 m) (Agarwal and Kumar 1973). The study area is characterized by deeply incised river valleys with the average annual precipitation of 1500 ± 300 mm, with most of it falling during the Indian Summer Monsoon season (Jamir et al. 2020).

The study area is situated in the transition zone between the Higher Himalaya and the Lesser Himalaya, demarcated by the NW–SE trending Main Central Thrust (MCT), locally known as the Munsiri Thrust. This MCT fault is generally a ~10–12 km thick, NNE dipping high strain ductile shear zone, which is referred to as the “MCT Zone” (Searle et al. 1993; Singh and Thakur 2001; Bhattacharya and Weber 2004, Srivastava and Tripathy 2007). The landslide is situated in the hanging wall of the thrust zone, comprising medium- to high-grade metamorphic rocks (augen gneiss) of the Munsiri Formation. Toward the northern part of the landslide area, the slopes comprise massive augen gneiss exposures, while toward the southern part, the slopes display quartzitic outcrops. Due to the presence of a fault zone in the region, there is a high degree of rock fragmentation, resulting in the formation of high frequency 3–4 joint sets outside the flanks of landslide, which are as follows: J1: (55° Dip/355° N Dip direction), J2 (20/65), J3 (40/320), J4 (35/200). These joint sets’ orientations have been used further as per “Slope stability”. The fractured zone decreases with distance from the landslide area. This is further discussed in “Structural controls on the Landslide”. The landslide section, prior to the slide, comprises sparsely distributed coniferous trees in the northern part of the slope, while the Southern part was marked by the Yamuna River, flowing E-W (Fig. 2a).

The Wazri landslide is complex in nature with a combination of debris and boulders, while the loose landslide debris material to date remains suspended on the steep

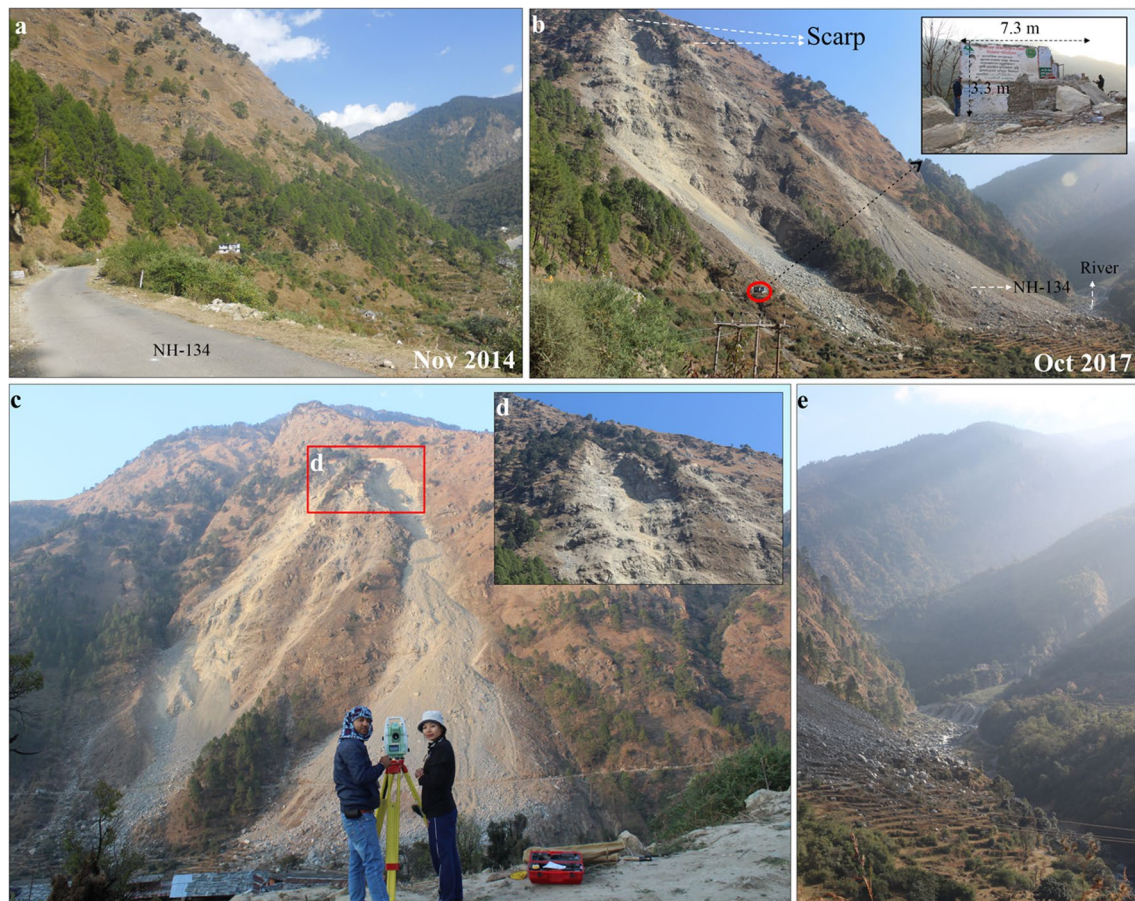


Fig. 2 Pre vs. post-failure conditions. **a** Pre-failure slope (Nov. 2014). **b** Post-failure slope (October 2017). Scale is represented by the area (24.09 m^2) of a house damaged by the slope failure. **c** Front view of

Wazri Landslide showing deposited material on both flanks and Total station (Leica TCR 1201+) survey. **d** Enlarged view of landslide scarp. **e** Landslide material reaching river floor

slope and is susceptible to further movements. The crown of the landslide is at an elevation of 2426 m, while the toe is at the Yamuna River at an elevation of 1719 m. The slope angle is $60\text{--}75^\circ$ approx. and undulatory. The 2017 failure had taken place on both flanks of the landslide area, with the landslide material being deposited up to the river floor, while the center portion of the slide zone still remains intact (Fig. 2b–e). Post failure, further material movements in the landslide area have been reported by local/national media (IANS 2019b), which still continued to disrupt the traffic and daily activity of the villagers in the vicinity of the landslide area, since it is the only route that connects the villages along the river valley. During field visits in September 2014 in this region, there were visible signs of creeping and remains of old landslide (paleo-landslide) (Fig. 3a, b). There were gullies located on both flanks of the present slide area (Fig. 3c, d). Several creep zones were identified above and below the road, along the entire stretch of the landslide area.

Methodology

Data collection

Satellite Imagery (Cartosat-1) and field assessment were used to finalize the location of 2D slope sections to be used in slope stability modeling. The Cartosat-1 Digital Elevation Model (DEM) with 10 m spatial resolution was prepared using the Cartosat-1 stereo image, which was used to extract the slope geometry. The pre-failure topography was based on Cartosat-1 DEM, whereas post-failure topography was constructed using Total-Station (Leica TCR 1201+ having 1" horizontal/vertical accuracy) survey on 10 October, 2017. Post-failure topography was constructed using interpolation of various survey points having x, y, z dimensions. The rock/soil samples, collected from the landslide, were analyzed in the National Geotechnical Facility (NGF), India. The rock samples were tested for Unconfined Compressive Strength (UCS) (IS:



Fig. 3 Pre-failure (Oct. 2014) observations. **a** Field photograph (Nov. 2014) of creeping and tilting trees. **b** Paleo-landslide material (boulders mixed in silty sand matrix). **c** Google Earth imagery showing

two gullies on the slope with the one on the southern side relatively larger (red dotted ellipses). **d** Field photograph (Nov. 2014) depicting erosional conditions at the left gully

9143-1979) and ultrasonic tests (CATS Ultrasonic (1.95) of Geotechnical Consulting & Testing Systems). The ultrasonic test was conducted to determine the density, elastic modulus, and Poisson's ratio of rock samples. The soil samples were tested for grain size (IS: 2720-Part 4: 1985), UCS test (IS: 2720-Part 10: 1991), and direct shear test (IS: 2720-Part 13: 1986).

Slope stability

In view of the complex nature of the landslide involving debris cover and big boulders and rock exposure near flanks, slope stability analysis involved stereonet-based Kinematic Analysis (Hoek and Bray 1981) and Finite Element Method (FEM)–Shear Strength Reduction (SSR) (Griffiths and Lane 1999) technique-based stability simulation. Kinematic analysis was performed using Dips (v 8.025) software to determine the potential role of joint plane roles in rockfalls and the FEM-SSR methods were applied using RS2 (v 11.021) software to determine the

overall stability of the hillslope and potential zones of stress/displacement.

In the FEM-SSR technique, the boundary conditions with restrained movement in X–Y directions were used for the base and back of the 2D models. In-situ field stress was adjusted in view of compressional stress, as the study area is situated in the vicinity of thrust fault zone (Fig. 1). The properties of the soil and rock mass were based on Mohr–Coulomb (M-C) and the Generalized Hoek–Brown (Hoek and Brown 1997) material models, respectively. Plane strain triangular elements having 6 nodes were used through the graded mesh in the models. Details of the criteria and input parameters used in the FEM analysis are mentioned in Table 1. To understand the uncertainty caused by the selection of 2D slope section, multiple slope sections were taken (Fig. 1). Rainfall infiltration (vertical) was also applied in the upper part of models based on high rainfall event (20 mm/3 h) on 23rd Sep. 2017 in the region.

Table 1 Details of criteria and input parameters for the FEM-based slope stability analysis

Material	Material criteria	Parameters*	Source	Value
Quartzite	Generalized Hoek and Brown (GHB) Criteria (Hoek et al. 1995) $\sigma_1 = \sigma_3 + \sigma_{ci} [m_b (\sigma_3 / \sigma_{ci}) + s]^a$ Here, σ_1 and σ_3 are major and minor effective principal stresses at failure; σ_{ci} , compressive strength of intact rock; m_b , a reduced value of the material constant (m_i) and is given by $m_b = m_i e^{[(GSI-100)/(28-14D)]}$ s and a are constants for the rock mass given by the following relationships; $s = e^{[(GSI-100)/(9-3D)]}$ $a = \frac{1}{2} + \frac{1}{6} \left[\frac{1 - e^{-(\frac{GSI}{15})}}{1 - e^{-(\frac{20}{3})}} \right]$ Here, D a factor which depends upon the degree of disturbance to which the rock mass has been subjected by blast damage and stress relaxation. GSI (Geological Strength Index); a rockmass characterization parameter	Unit weight (MN/m ³) Uniaxial Compressive Strength Young's Modulus (Ei), MPa Poisson Ratio Peak Geological Strength Index Residual Geological Strength Index Material constant (mi) mb (peak) mb (residual) s (peak) s (residual) a (peak) a (residual) D (peak) D (residual)	Laboratory analysis (UCS) (IS: 9143-1979) Laboratory analysis (ultrasonic velocity test); Hoek and Diederichs (2006) Field observation and based on recent amendments (Cai et al. 2007 and reference therein) Standard values (Hoek and Brown 1997) GSI was field dependent, mi as per (Hoek and Brown 1997) and D is used between 0 and 1 in view of rockmass exposure and blasting	0.028 170 25,000 0.27 41.51 17.8 20 2.4766 1.0617 0.0015 0.0001 0.5103 0.5506 0.5 0.5
Joints	Barton-Bandis Criteria (Barton and Choubey 1977; Barton and Bandis 1990) $\tau = \sigma_n \tan [\phi_j + JRC \log_{10} (JCS/\sigma_n)]$ Here, τ is joint shear strength; σ_n , normal stress across joint; ϕ_j , reduced friction angle; JRC, joint roughness coefficient; JCS, joint compressive strength. The JRC is based on the chart of Barton and Choubey (1977); Jang et al. (2014). JCS was determined using following equation: $\log_{10}(JCS) = 0.00088 (R_L)(\gamma) + 1.01$ Here, R_L is Schmidt Hammer Rebound value and γ is unit weight of rock. The JRC and JCS were used as JRC _n and JCS _n following the scale corrections observed by Barton and Choubey (1977) and reference therein $JRC_n = [JRC(L/L_0)]^{\gamma} \{-0.02(JRC)\}$ $JCS_n = [JCS(L/L_0)]^{\gamma} \{-0.03(JRC)\}$ Here, L and L ₀ are mean joint spacing in field, respectively. L ₀ has been suggested to be 10 cm Joint stiffness criteria (Barton 1972) $k_n = (E_i^* E_m) / L_e (E_i - E_m)$ Here, k_n is Normal stiffness, E_i Intact rock modulus, E_m Rockmass modulus, L Mean joint spacing $E_m = (E_i)^* [0.02 + \{1 - D/2\} / \{1 + e^{(60+15^*D-GSI)/11}\}]$ Here, E_m is based on Hoek and Diederichs (2006) and reference therein	Normal Stiffness (kn), MPa/m Shear stiffness (ks), MPa/m Scale-corrected JRCn Scale-corrected JCSn, MPa	Ei is lab dependent and GSI was field dependent. D is used between 0 and 1 in view of rock mass exposure and blasting It is assumed as kn/10. However, effect of denominator is also obtained through parametric study Field-based data from profilometer and standard values from Barton and Choubey (1977); Barton and Bandis (1982); Jang et al. (2014) Empirical equation of Deere and Miller (1966) relating Schmidt Hammer Rebound (SHR) values, σ_{ci} and unit weight of rock. SHR was field dependent. Correction as per Barton and Bandis (1982)	11,405.5 4251.1 15,587.5 20,783.3 1140.6 425.1 1558.8 2078.3 5.86 5.13 6.11 6.35 128.89 105.70 137.24 145.41

Table 1 (continued)

Material	Material criteria	Parameters*	Source	Value
Soil	Mohr–Coulomb Criteria (Coulomb 1776; Mohr 1914) $\tau = C + \sigma \tan \phi$ Here, τ is Shear stress at failure, C Cohesion, σ_n normal strength, ϕ angle of friction	Unit Weight (MN/m ³) Young's modulus (MPa) Poisson's ratio Cohesion, C (MPa) Angle of friction, ϕ (degree)	Laboratory analysis (UCS) (IS: 2720-Part 4-1985; IS: 2720-Part 10-1991) Laboratory analysis (UCS); IS: 2720-Part 10-1991 Standard values from Bowles (1996) Laboratory analysis (Direct shear) (IS: 2720-Part 13-1986)	0.021 60 0 31

Climatic regime

The study area is situated in the NW Himalaya that receives precipitation from the Indian Summer Monsoon and Western Disturbance. To determine and validate the role of precipitation in triggering the landslide, rainfall patterns were studied at monthly, daily, and 3-hourly scales by extracting dataset from [https://giovanni.gsfc.nasa.gov/giovanni/\(NASA2021\)](https://giovanni.gsfc.nasa.gov/giovanni/(NASA2021)). Apart from rainfall, soil moisture and surface runoff pattern were also explored because they both owe their origin to precipitation (rainfall) with varying degree of correlation, as also noted by Kumar et al. (2021a). Monthly and daily rainfall, surface runoff, and soil moisture data, which were used in the present study are based on the FLDAS (Famine Early Warning Systems Network Land Data Assimilation System) model (McNally et al. 2017). It employs precipitation datasets and analyses like CHIRPS (Climate Hazards Group Infrared Precipitation with Station data) & MERRA2 (Modern-Era Retrospective analysis for Research and Applications, Version 2) along with land cover data to derive variables like soil moisture and runoff. 3-hourly dataset of these parameters is based on GLDAS (Global Land Data Assimilation System) model (Beaudoin and Rodell 2020). It utilizes Global Data Assimilation System (GDAS) atmospheric analysis fields, daily analysis precipitation fields and the Air Force weather agency's Agricultural Meteorological Modeling System (AGRMET) radiation fields.

Rockfall simulation

In view of the 12 September, 2017 rockfall event in the landslide that damaged ~ 400 m stretches of the NH-134 road and isolated the people of 12 villages in the region, rockfall simulation was also performed to determine the characteristics of a potential rockfall event that may strike the road passing through the landslide. It is also evident from the 2018 and 2021 GE images that there is activation of minor scarps within the landslide body (Fig. 9c, d). The evident scarp zone (Fig. 9d) of landslide, exposed to extreme rainfall events, further increases the possibility of such event. Rockfall simulation was performed using RAMMS software that employs a 3D terrain based rigid body–hard contact model to simulate the rockfall trajectories based on Leine et al. (2014). Though there are other 3D models that have been used in the last decade (Dubois et al. 2011), the RAMMS-based rockfall simulation has been preferred owing to the ability to model rigid polyhedron bodies and hard contacts. The terrain contact is assumed to be impenetrable and attains elastic equilibrium between rigid polyhedron rock and rigid contact by Signorini Law (Leine et al. 2014). The simulator can account for sliding, rolling and/or jumping motions of rocks in contact with the terrain (Leine et al. 2014).

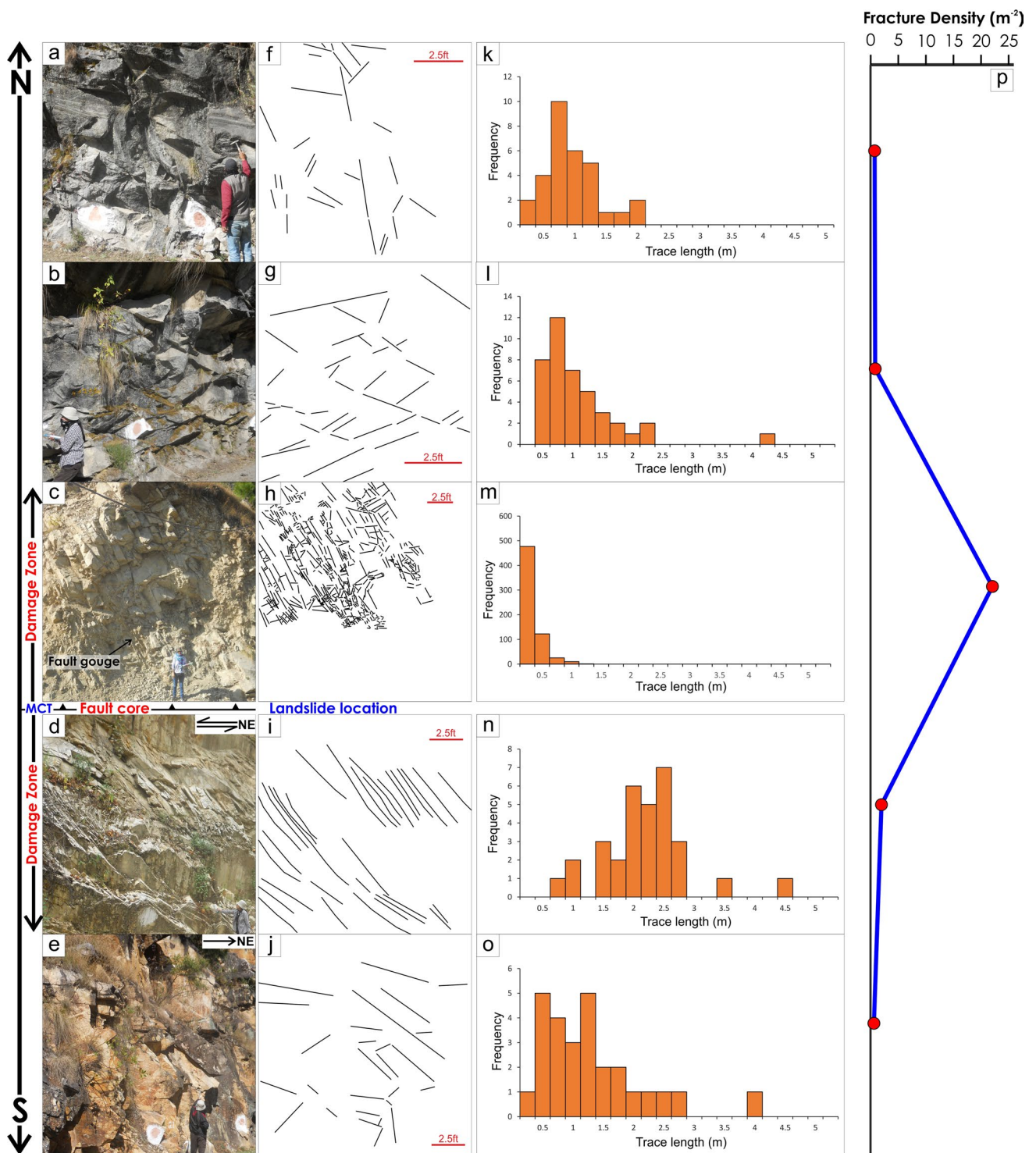


Fig. 4 a–e Field photograph of fractures across the MCT zone that includes quartzite in the footwall and gneiss in the hanging wall. The MCT zone is subdivided into fault core, damage zone, and intact zone that is devoid of brittle fracturing. f–j Traced fractures from the field

photographs. k–o Histograms of fracture trace length. p Fracture density is estimated from the traced fractures presented in f–j following the equations of Mauldon et al. (2001) using the FracPaQ MATLAB package (Healy et al. 2017)

Structural analysis

To analyze the role of deformation in the landslide, the study area has been subdivided into three distinct zones: (i) fault core, (ii) fault damage zone, and (iii) the intact zone (undeformed host rock), based on field data. This categorization, though not unique, remains crucial for deciphering the influence of structures on diverse phenomena like landslides, groundwater movement, and earthquake behavior (e.g., Billi et al. 2003; Ojha et al. 2022; Pradhan et al. 2022). Further, to assess the effect of the fractures, fracture density along with fracture trace lengths were calculated across the MCT zone, encompassing the MCT fault core, damage zone, and the intact zone, both to the north and south of the MCT (Fig. 4a–e). This analysis includes both the footwall and the hanging wall of the MCT. All the fractures were traced manually using graphic designing software from the field photographs (Fig. 4f–j). Traced fractures from the field photographs were further analyzed to estimate the fracture density following the equations of Mauldon et al. (2001) and trace length in the FracPaQ MATLAB package (Healy et al. 2017).

Results

Slope stability analysis

Kinematic analysis revealed that existing joint orientations do not result in planar and/or wedge failure (Fig. 5). However, in case of decrease in friction angle, currently critically intersection points that are lying outside of critical failure zone might come in failure zone. Such decrease in friction

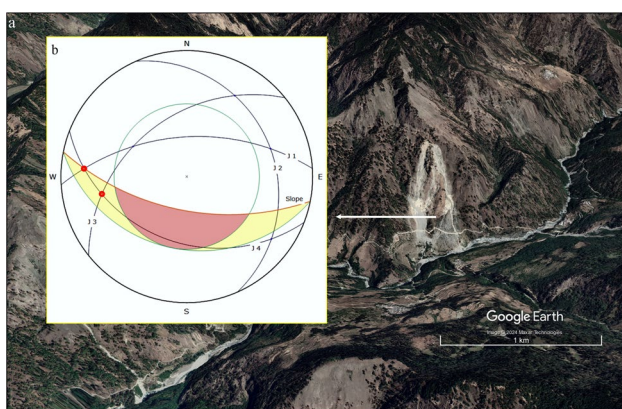


Fig. 5 Results of the Kinematic analysis. **a** Regional setting of the study area comprising study area landslide. Image Copyright: Google Earth. **b** Kinematic analysis of the joints (J1–J4) in landslide rock mass. Green circle represents friction angle (30°), whereas pink zone refers to critical zone. Red points at the joint intersections represent critical intersection

angle might occur during rainfall as also noted in other studies (Kumar et al. 2019).

To evaluate the hillslope response, slope stability analysis was performed for both pre (back analysis)- and post-failure (prediction) topography conditions (Fig. 6). Here, pre-failure event refers to 12 Sep. 2017 failure that was triggered by antecedent rainfall (Sect. 1). Results showed that much strain and displacement are still accumulated in the existing slope topography (Fig. 6b, e, h, k). Under pre-failure topography condition, maximum shear strain of about ~ 0.14 to 0.18 developed parallel to the slope (Fig. 6d, j) and total displacement of about ~ 2 to 8 m was likely to take place, parallel to the slope (Fig. 6a, g). Post-failure topography condition (prediction) revealed that the slope is still unstable with maximum shear strain and total displacement in the range of ~ 0.07 to 0.15 and ~ 2 to 5 m, respectively (Fig. 6b, e, h, k). This is further evident from the overlapping total displacement and shear strain pattern in pre- and post-failure conditions (Fig. 6c, f, i, l). Notably, during pre-failure analysis, slope section CS-2 was more unstable, whereas during post-failure analysis, the CS-1 has revealed more instability.

This behavior can be justified from the notion that after slope failure, the CS-2 has achieved relatively less steep topography than the CS-1 slope section. The accumulated displacement and strain, predicted in the post-failure topography, can be partially validated by the slope failure incident in this slope on July 11, 2018, due to incessant rainfall, resulting in the disruption of the daily traffic and stranding ~ 90 to 100 pilgrims of the Char Dham Yatra (IANS 2018). Such accumulated displacement and strain could be attributed to the slope steepness ($> 60^\circ$) and highly sheared rock mass in the landslide zone. As noticed in pre-failure topography analysis, the landslide zone had developed shear strain parallel to the slope (Fig. 6d, j) that finally resulted into failure on 12 September 2017. Field observations had also indicated creeping in the form of tilting of trees and cracks on the road passing through the landslide (Fig. 2d). Notably, such creeping has been attributed as indications of progressive strain development in many studies (Terzaghi 1950; Varnes 1978).

Rainfall as a triggering mechanism

To determine the role of rainfall as a triggering mechanism and the possibility of triggering another rockfall from the exposed scarp, rainfall patterns were explored. Monthly dataset of 1982–2020 revealed a temporal increase in the rainfall and associated climatic parameters (Soil Moisture, Surface Runoff) particularly after 2010 (Fig. 7a–c). Conspicuously, the year 2010 came with a dramatic shift in the El Niño–Southern Oscillation that possibly affected precipitation patterns in Southeast Asia, and particularly Himalaya (Stanley et al. 2020; <https://www.ncdc.noaa.gov/>

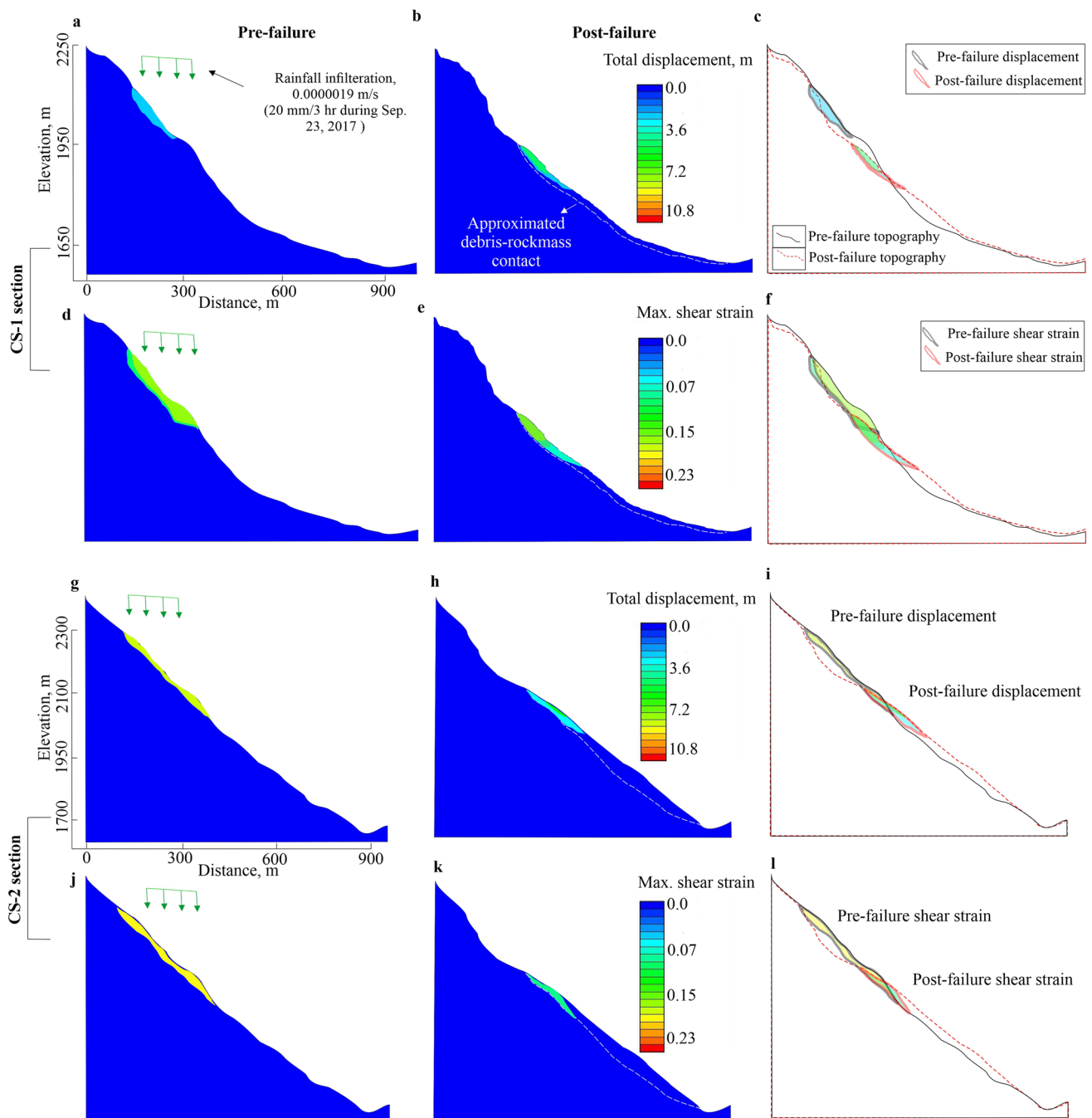


Fig. 6 Slope stability evaluations under pre- and post-failure conditions. **a–c** Total displacement in the CS-1 section and their merging/overlapping pattern in pre- and post-failure conditions; **d–f** maximum shear strain in the CS-1 section and their merging/overlapping pattern

in pre- and post-failure conditions; **g–i** total displacement in the CS-2 section and their merging/overlapping pattern in pre- and post-failure conditions; **j–l** maximum shear strain in the CS-2 section and their merging/overlapping pattern in pre- and post-failure conditions

[sotc/global/201013](https://doi.org/10.1007/s12665-021-10103-3), accessed on 19 Feb. 2021). Further, daily rainfall data in different months of the year 2017 revealed relatively higher values in September (Fig. 7d). The analysis for daily rainfall data and other parameters was specifically chosen for the year 2017 after surveying reports and discussing with residents of the nearby

village who reported incessant rainfall in September, 2017. Further, to better understand the role of rainfall as a triggering factor, 3-hourly rainfall data from 1 August to 30 September was explored (Fig. 8a). Though the first slope failure occurred on 12 September 2017, rainfall data of August were analyzed in view of various studies that have

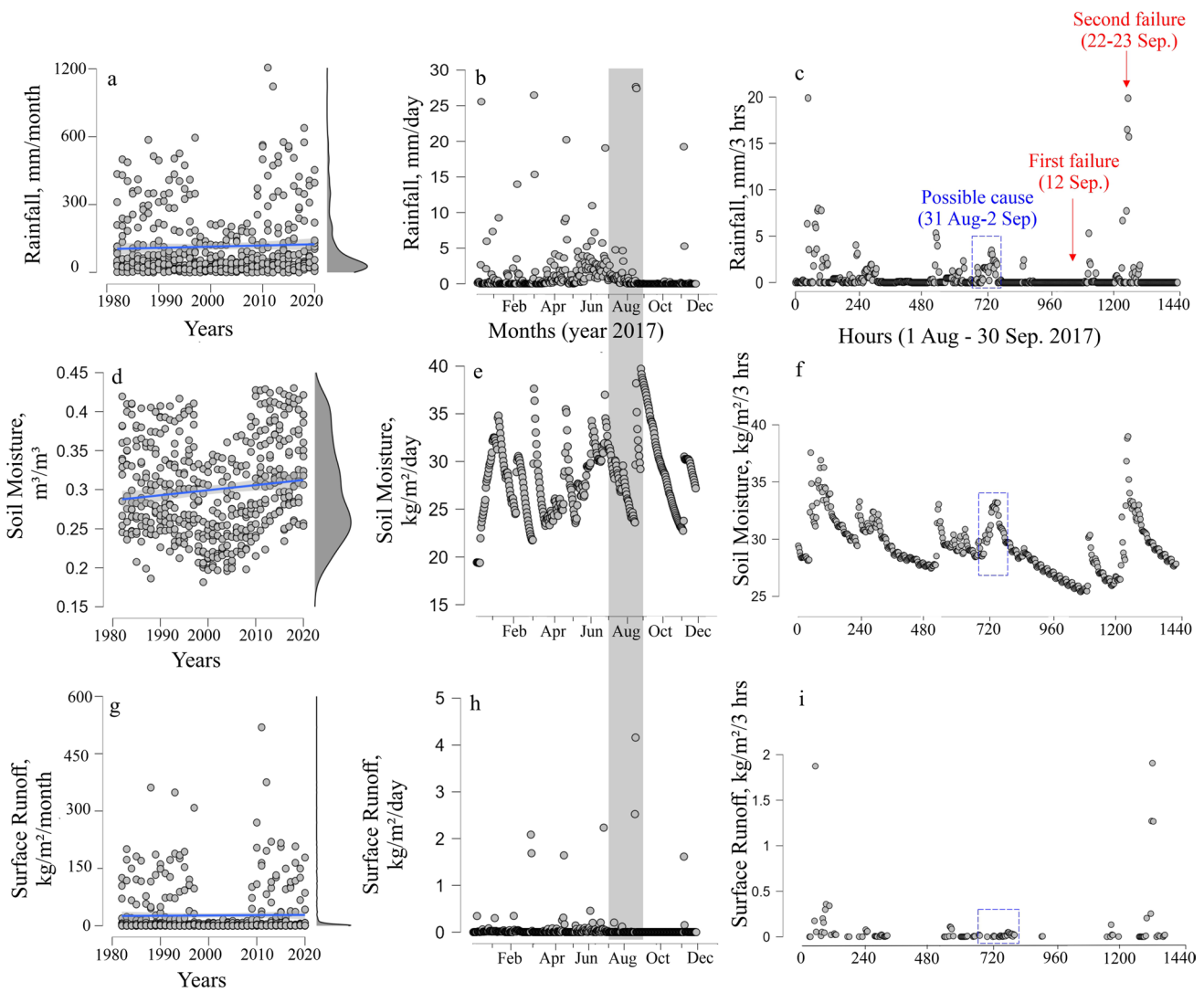


Fig. 7 Rainfall and associated parameters regime in study area. **a–c** Rainfall, soil moisture and surface runoff variation at monthly scales for 1980–2020; **d–f** rainfall, soil moisture and surface runoff variation at monthly scales for 2017. Source of monthly datasets during the years 1982–2020: FLDAS_NOAH01_C_GL_M model (McNally et al. 2017). Spatial resolution of dataset: 0.1° (~10 km). Source of

daily datasets: FLDAS_NOAH001_G_CA_D model (Jacob et al. 2021). Spatial resolution of dataset: 0.01° (~1 km). Gray bar in Fig. 6d–f highlight Aug–Sep daily pattern for which 3-hourly datasets are presented in a–d. The outliers in a–c represents extreme values in respective months for the respective parameters

observed the role of days–months antecedent rainfall in triggering landslide (Li et al. 2011).

It was noted that on the 12 September 2017, there was no rainfall event and similar finding corresponded to soil moisture and surface runoff (Fig. 8b, c). However, during 31 August–2 September 2017, a total ~33 mm rainfall occurred with corresponding increases in soil moisture and surface runoff. This may have acted as an antecedent triggering factor. The sudden increase in the groundwater runoff during 31 August–2 September 2017, in response to rainfall infiltration, further supports the notion of possible role of antecedent rainfall (31 August–2 September 2017) in the first slope failure of 12 September 2017 (Fig. 8d). Iverson

(2000), Brönnimann (2011) and Take et al. (2015) have also observed that rainfall induced groundwater pressure, even if antecedent, along the slope surface, contributes in the slope failure.

It is evident that the role of antecedent rainfall, soil moisture and/or groundwater in slope failure also depends upon existing slope morphology, shear strength of slope material, and material diffusivity (Iverson 2000). Field observations prior to the failure (October, 2014) indicated gully erosion on both flanks of the landslide body (Fig. 3c) that may also have contributed to the failure mechanism during rainfall. Unlike 12 September, 2017 event, the second failure that occurred on 22–23

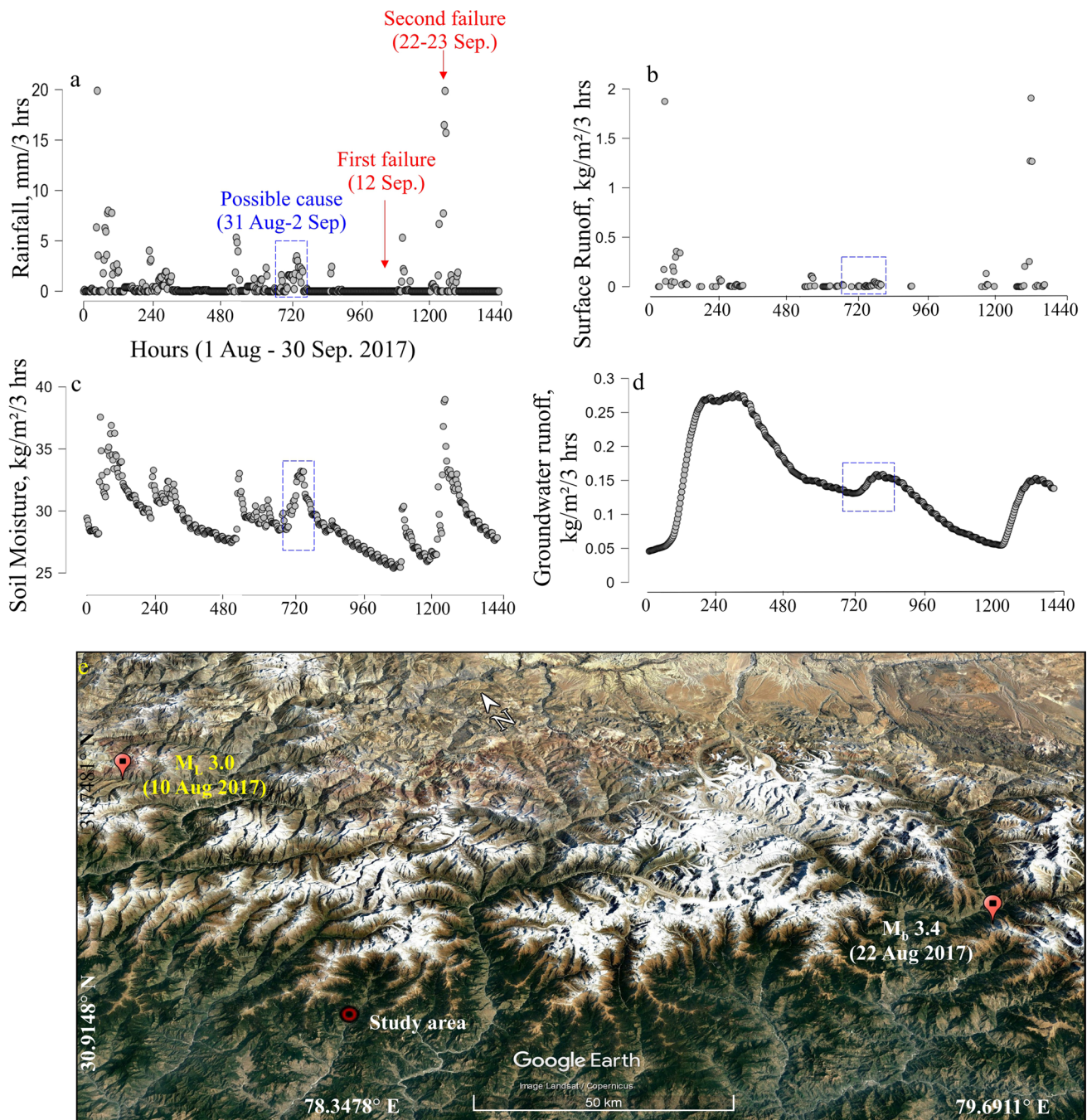


Fig. 8 Climatic and seismic pattern during Aug–Sep 2017. **a–d** 3-hourly variation of rainfall, surface runoff, soil moisture, and groundwater runoff. Spatial resolution of dataset: 0.01° (~1 km). Source of hourly datasets: GLDAS_NOAH025_3H model (Beaudou-

ing and Rodell 2020). Blue rectangle in Fig. 7a–d highlights possible cause (antecedent rainfall) of first slope failure. **e** Seismic events during Aug–Sep 2017. Data source: International Seismological Centre (2022), On-line Bulletin, <https://doi.org/10.31905/D808B830>

September 2017 was evident regarding the influence of extreme rainfall (> 50 mm/24 h), which was also visible in abnormally higher soil moisture and surface runoff. Apart from rainfall, the potential role of seismicity was also explored and it has been found that only 2 minor

seismic events ($3 < \text{earthquake magnitude} > 3.5$) occurred during August–September 2017 about 95–150 km away from study area (Fig. 8e). Hence the possibility of seismicity as a triggering factor was considered unlikely.

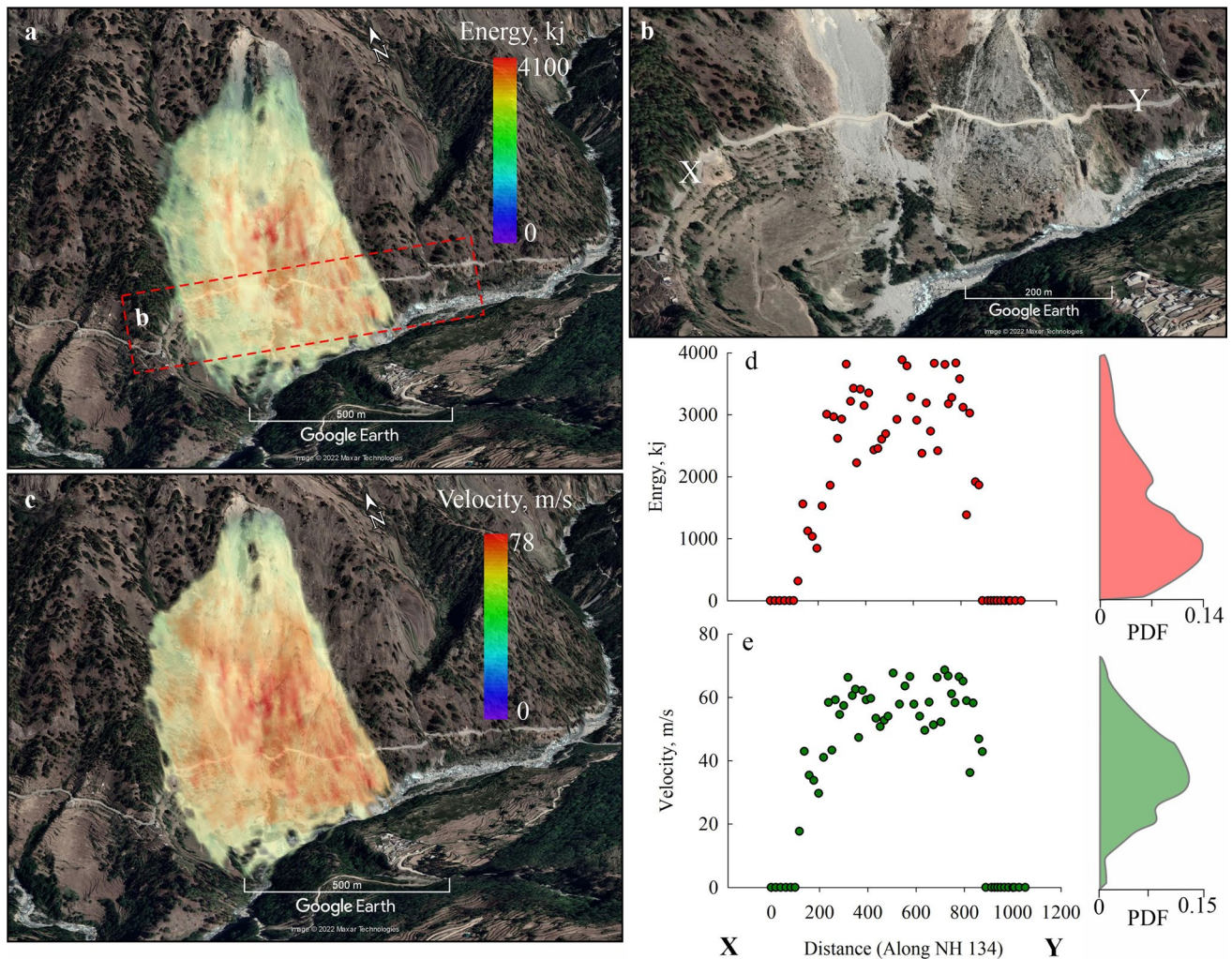


Fig. 9 Rockfall simulation. **a** Rockfall energy. **b** The NH road section along which energy and velocity variation is shown in **d–e**. **c** Rockfall velocity. **d–e** Variation of energy and velocity along with PDF (probability density function) pattern along the X–Y stretch of the NH road

Structural controls on the landslide

Deformation along a fault plays a critical role in controlling the rock strength and permeability, and hence controlling the slope stability and landslides (Bloom et al. 2022; Korup 2004; Upton et al. 2018). The Main Central Thrust (MCT) shear zone is a brittle–ductile shear zone, where the brittle fractures overprint the ductile shear fabrics (Fig. 4a–e). It is evident that the landslide is confined to the MCT core zone (Fig. 1a). Presence of fine-grain crushed cataclastic rocks, and fault gouge, predominate in the MCT fault core (Fig. 4c), are the characteristic signature of a fault core. As the fault core is the zone of crushed cataclastic rocks, it was discarded for the calculation of fracture density and fracture length. As we moved north and south of the fault core, a highly fractured rock volume marked the fault damage zone (Fig. 4m, p). The damage zone is characterized by low

fracture trace length and high fracture density (Fig. 4m, p). A few hundred meters to the north and south from the fault damage zone, the fractures are less abundant. The fracture density gradually decreases, and the fracture length gradually increases as we move away from the damage zone (Fig. 4k–o, p). The fracture trace length is least, with a peak fracture density (22 m^{-2}) close to the fault core (Fig. 4m, p).

The fracture trace length and fracture density analysis reveal a higher degree of brittle deformation in the area where the landslide was observed (Fig. 4). The higher degree of fracture density with a minimum fracture trace length highlights the effect of tectonic deformation-related structures along the MCT zone in the landslide. High fracture density along with the fault gouge maximizes permeability and minimizes the rock cohesion and hence provides a suitable location for the landslide. Similar work has also been carried out by Scheingross et al. (2013) in the San Andreas

Fault, Central California, where they hypothesized that the fault damage zone, which contributes to erosional processes, may be favorable to slow-moving landslides due to high density of fractures and deteriorated rock strength. The role of lithology has been ruled out from this case study since the landslide zone is confined to the high-grade augen gneiss of Higher Himalaya. However, the degree of deformation and shearing in the landslide zone is highly indicative of tectonic disturbance, which stimulates destabilization of the rock mass and infiltration of superficial water. All these conditions, aided by the steep topography of the slope, collectively contributed to the slope failure.

Potential rockfall characteristics

Potential rockfall events are presented through the energy and velocity characteristics and their respective probability density function (PDF) (Fig. 9a, c). The simulation revealed energy and velocity in the range of 1200–4100 kJ and 20–78 m/s, respectively in the landslide body and around it. The NH-134 road, passing through the landslide also gets struck by this potential rockfall with the energy and velocity in the range of 900–4000 kJ and 18–75 m/s, respectively (Fig. 9b, d, e). The PDF estimates along the X–Y stretch of the road reveal the likelihood to get struck by 600–1000 kJ energy and 25–35 m/s velocity of rockfall event. Notably, the rockfall event is considered to occur again in view of the exposed scarp of September 2017 landslide event that damaged a ~400 m stretches of the road and a house measuring

24 m² (plan area) in dimension. The antecedent rainfall that is inferred to be responsible for 12 Sep 2017 event might cause such failure again as the extreme rainfall events are becoming more frequent in the study area ("[Rainfall as a triggering mechanism](#)"). Krautblatter and Moser (2009), Ansari et al. (2015), and Melillo et al. (2020) have also observed the role of extreme/consistent rainfall in the rockfall triggering in different mountain systems.

Finally, since the study also aims to give insight into possible landslides in the future, it is necessary to include its evolution over the past few years to evaluate recurrence. In the year 2012, the gullies that existed on the left and right flank of the slope prior to the failure were $4368.17 \pm 48 \text{ m}^2$ and $21,708.1 \pm 238 \text{ m}^2$, respectively (Fig. 10a) that increased to $6382.37 \pm 70 \text{ m}^2$ and $22,555.8 \pm 248 \text{ m}^2$ in the year 2016 (Fig. 10b). Post failure in 2017, a large degree of the debris material remained suspended in the slope. The landslide area had increased to $244,734.8 \pm 2692 \text{ m}^2$ (Fig. 10c). Subsequently, the areal extent of the landslide has reduced to $234,191.3 \pm 2576 \text{ m}^2$, as the suspended debris material gradually got washed out from the slope during the rainfall events (Fig. 10d). Post-failure in 2017, a large degree of the debris material remained suspended in the slope. The landslide area had increased to $244,734.8 \pm 2692 \text{ m}^2$ (Fig. 10c). Subsequently, the areal extent of the landslide has reduced to $234,191.3 \pm 2576 \text{ m}^2$, as the suspended debris material gradually got washed out from the slope during the rainfall events (Fig. 10d).

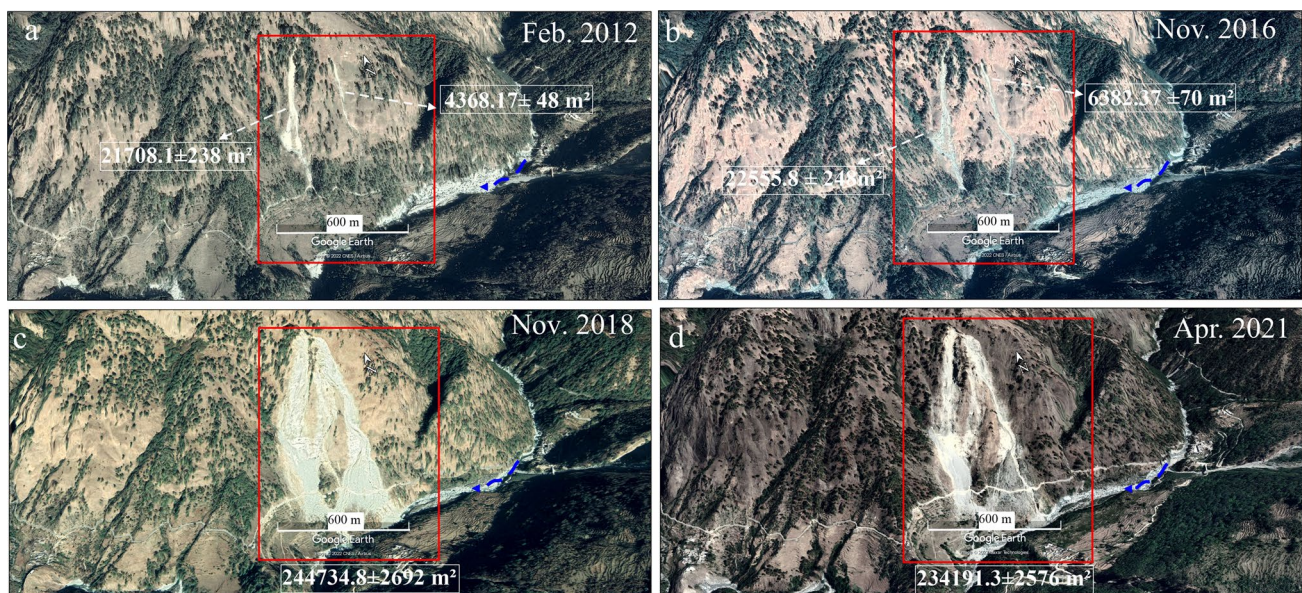


Fig. 10 Areal evolution of Wazri landslide. **a** Feb. 2012. **b** Nov. 2016. **c** Nov. 2018. **d** Apr. 2021. Red rectangle refers to study area. Blue arrow represents river flow direction. Data source: Google Earth

imagery. Error in values correspond to mapping error (1.10%) determined by comparing Google earth distance with random known distances in the study area

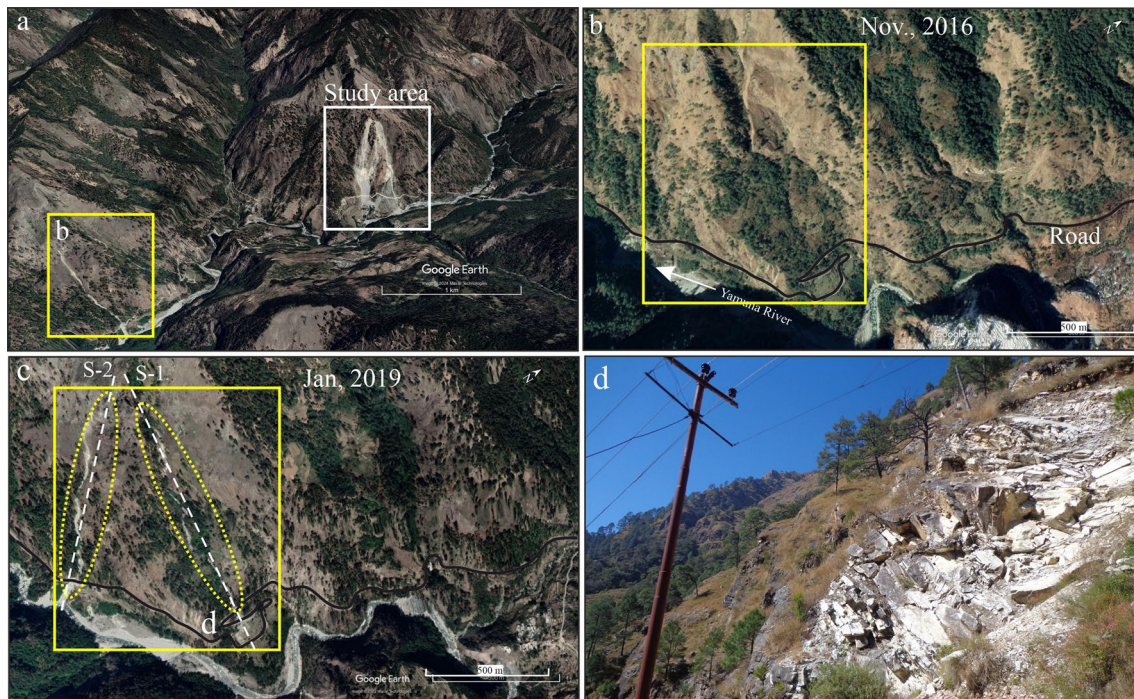


Fig. 11 **a** Regional setting location of the study area and Silai bend hillslope (**b**). **b** Google Earth image of Silai Bend hillslope (Nov. 2016). **c** Google Earth image of Silai Bend hillslope (Jan. 2019). Yel-

low dashed ellipse demarcates formation of gullies. S-1 and S-2 are slope sections that are taken for FEM-SSR slope stability analysis (results in Fig. 12). **d** Highly sheared quartzite rock mass

Finally, a similar pattern, as in case of study area landslide, has also been observed at Silai bend, 2 km downstream from the Wazri landslide where gullies have developed during 2016–2019 (Fig. 11a, b). Sheared rock mass, tilted trees are already indicative of creeping as observed in the field (Fig. 11c, d). Four joint sets in the exposed rock mass at the flank of hillslope have following dip amount and dip direction: J1 ($45^{\circ}/70^{\circ}$ N), J2 ($70^{\circ}/220^{\circ}$ N), J3 ($80^{\circ}/40^{\circ}$ N), J4 ($85^{\circ}/350^{\circ}$ N).

Further, slope stability analysis of two sections S1 and S2 indicated an accumulated shear strain of 0.08–0.02 parallel to the slope, with a critical SRF of 1.09–1.24 (Fig. 12). Further, kinematic analysis also reveals wedge failure condition caused by J1 and J4 joint set intersection (Fig. 12c).

Discussion

This study employed instability and rockfall simulations to comprehensively evaluate the failure regime of an active landslide in the NW Himalaya. The findings highlight the crucial role of rainfall in triggering landslides, particularly when coupled with pre-existing instability caused by factors like tectonic structures and steep slopes. The study emphasizes the importance of considering antecedent rainfall and

its impact on hillslope material moisture regime, as these can contribute to failure even in the absence of immediate rainfall events. Furthermore, the link between tectonic structures and landslide is underscored by the presence of the landslide within the Main Central Thrust core zone, characterized by high fracture density and permeability. The potential for future rockfalls is concerning, especially considering the impact on the nearby road. The predicted energy and velocity values highlight the need for mitigation measures to protect infrastructure and ensure public safety. The ongoing expansion of gullies and concerning slope stability at the adjacent Silai bend hillslope further emphasize the importance of continuous monitoring and proactive measures to prevent future landslides in the region.

While the study provides valuable insights, limitations include lack of direct validation data for some parameters. Future work involves field monitoring of rockfalls and slope movements, incorporating real-time rainfall data into simulations, and exploring the influence of additional factors like vegetation and human activities. Nonetheless, the findings provide valuable insights into the failure mechanisms and highlight the critical role of rainfall and tectonic structures in slope failure that pose significant socio-economic risk to the nearby community.

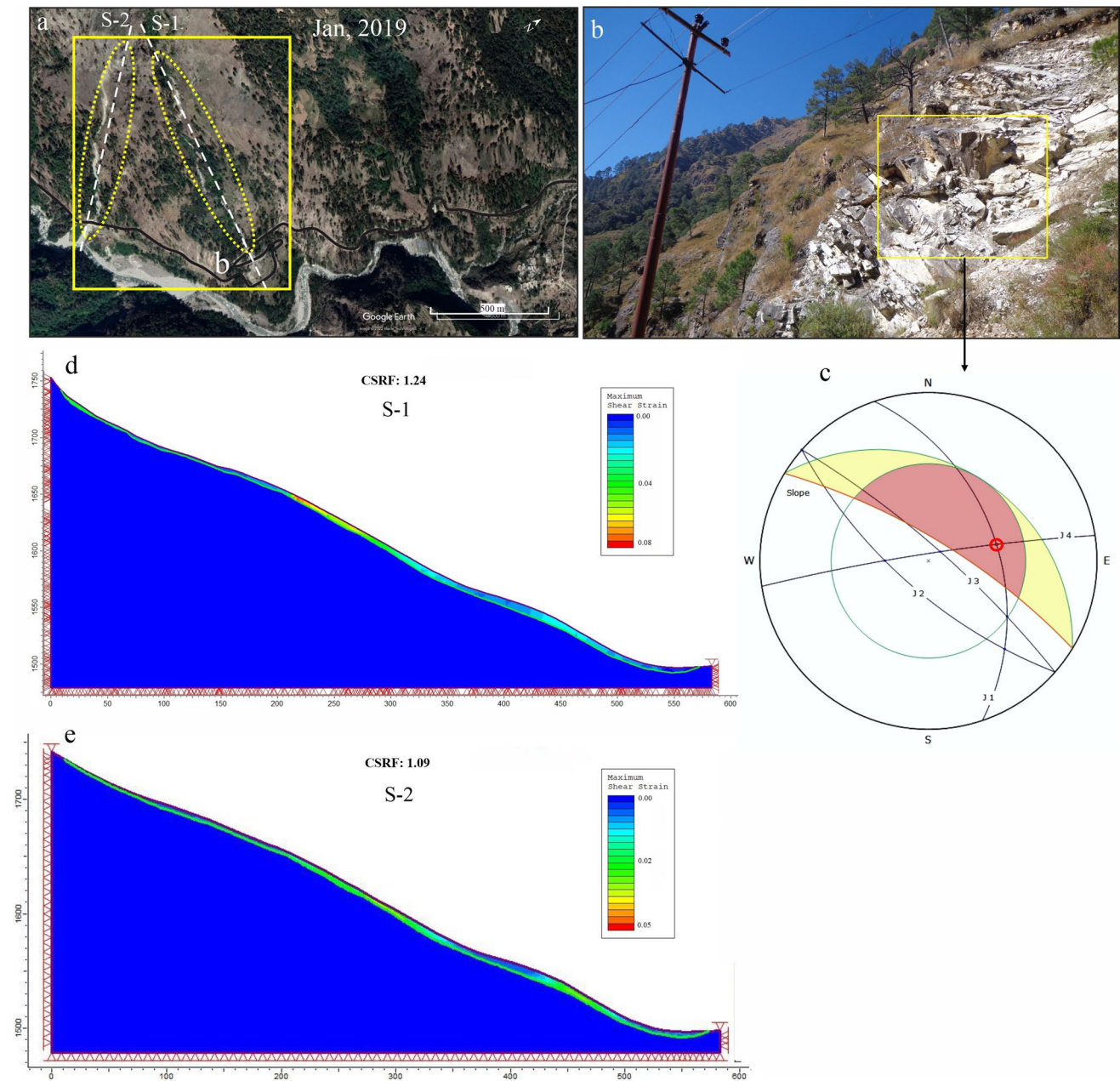


Fig. 12 Slope stability evaluation of Silai Bend hillslope. **a** Google Earth image of Silai Bend hillslope (Jan. 2019). S-1 and S-2 are slope sections that are taken for FEM-SSR slope stability analysis. **b** Highly sheared quartzite rock mass. **d–e** Maximum shear strain and critical strength reduction factor in the S-1 and S-2 section respectively.

c Kinematic analysis of the joints (J1–J4) in landslide rock mass. Green circle represents friction angle (30°), whereas pink zone refers to critical zone. Red points at the joint intersections represent critical intersection

Conclusion

This study employed a combined approach of instability and rockfall simulations to investigate the failure regime of an active landslide in the NW Himalaya. The findings reveal a complex interplay between pre-existing instability factors (e.g., steep slopes, tectonic structures) and rainfall

as the primary trigger for landslides. Key conclusions are as follows: rainfall, particularly antecedent events, plays a critical role in triggering landslides even without immediate rainfall, tectonic structures like the MCT zone influence landslide recurrence through increased fracture density and permeability, the landslide remains unstable with potential for future rockfalls impacting the nearby road

(energy 900–4000 kJ, velocity 18–75 m/s), gully expansion and concerning slope stability at Silai bend suggest potential for future landslides there. This study contributes valuable insights into the complex mechanisms governing landslide failure in the NW Himalaya. The identified potential for future landslides underscores the need for continuous monitoring and proactive mitigation strategies to ensure public safety and infrastructure integrity.

Acknowledgements IJ is thankful to Director, CSIR-National Geophysical Research Institute, Hyderabad (India) for consistent support. We are thankful to Editor Prof. Mihai Ciprian Margarint and two anonymous reviewers for their constructive comments and suggestions.

Author contribution IJ, DVG, and VK conceived the idea. IJ and VK performed the field data collection and laboratory analysis. IJ, VK, DVG, VG, and TRM contributed in the numerical simulations. IJ and AKO interpreted the fracture pattern. All authors contributed to the writing of the final draft.

Funding This work was supported by the Department of Science and Technology, Government of India, New Delhi [INSPIRE fellowship IF130881].

Data availability Though most of the dataset has been provided in the MS and table, additional raw datasets can be provided, if requested.

Declarations

Conflict of interests The authors declare that they have no conflict of interests.

References

- Agarwal NC, Kumar G (1973) Geology of the upper Bhagirathi and Yamuna Valleys, Uttarkashi district, Kumaun Himalaya. *Himalayan Geol* 3:2–23
- Alexander D, Formichi R (1993) Tectonic causes of landslides. *Earth Surf Proc Land* 18(4):311–338
- Ansari MK, Ahmed M, Rajesh Singh TN, Ghalayani I (2015) Rainfall, a major cause for rockfall hazard along the roadways, highways and railways on hilly terrains in India. *Engineering geology for society and territory*. Springer, Cham, pp 457–460
- Bălteanu D, Micu M, Jurchescu M, Malet JP, Sima M, Kucsicsa G et al (2020) National-scale landslide susceptibility map of Romania in a European methodological framework. *Geomorphology* 371:107432. <https://doi.org/10.1016/j.geomorph.2020.107432>
- Barton NR (1972) A model study of rock-joint deformation. *Int J Rock Mech Mining Sci Geomech Abstr* 9(5):579–602
- Barton N, Choubey V (1977) The shear strength of rock joints in theory and practice. *Rock Mech* 10(1–2):1–54
- Barton N, Bandis S (1982) Effects of block size on the shear behavior of jointed rock. In: *Proceedings of the 23rd US Symposium on Rock Mechanics*. vol. 2, pp. 739–760. American Rock Mechanics Association
- Barton NR, Bandis SC (1990) Review of predictive capabilities of JRC–JCS model in engineering practice. In: Barton N, Stephansson O (eds) *Rock joints*. Rotterdam, pp. 603–610
- Beaudoing H, Rodell M (2020) NASA/GSFC/HSL, GLDAS Noah Land Surface Model L4 3 hourly 0.25 × 0.25-degree V2.1. Greenbelt, Maryland, USA: Goddard Earth Sciences Data and Information Services Center (GES DISC)
- Bhattacharya AR, Weber K (2004) Fabric development during shear deformation in the Main Central Thrust zone, NW-Himalaya, India. *Tectonophysics* 387(1–4):23–46. <https://doi.org/10.1016/j.tecto.2004.04.026>
- Billi A, Salvini F, Storti F (2003) The damage zone–fault core transition in carbonate rocks: implications for fault growth, structure and permeability. *J Struct Geol* 25(11):1779–1794. [https://doi.org/10.1016/S0191-8141\(03\)00037-3](https://doi.org/10.1016/S0191-8141(03)00037-3)
- Bloom CK, Howell A, Stahl T, Massey C, Singeisen C (2022) The influence of off-fault deformation zones on the near-fault distribution of coseismic landslides. *Geology* 50(3):272–277. <https://doi.org/10.1130/G49429.1>
- Bowles JE (1996) *Foundation analysis and design*, 5th edn. McGraw-Hill, New York
- Brönnimann CS (2011) *Effect of groundwater on landslide triggering*. EPFL. <https://doi.org/10.5075/epfl-thesis-5236>
- Cai M, Kaiser PK, Tasaka Y, Minami M (2007) Determination of residual strength parameters of jointed rock masses using the GSI system. *Int J Rock Mech Min Sci* 44(2):247–265
- Cascini L, Fornaro G, Peduto D (2009) Analysis at medium scale of low-resolution DInSAR data in slow-moving landslide-affected areas. *ISPRS J Photogramm Remote Sens* 64(6):598–611. <https://doi.org/10.1016/j.isprsjprs.2009.05.003>
- Coulomb CA (1776) *Essay on an application of the rules of maximis and minimis to some problems of statics*. Acad Memoirs R Sci 7
- Cui S, Pei X, Huang R (2018) Effects of geological and tectonic characteristics on the earthquake-triggered Daguangbao landslide. *China Landslides* 15(4):649–667. <https://doi.org/10.1007/s10346-017-0899-3>
- Deere DU, Miller RP (1966) *Engineering classification and index properties for intact rock*. Illinois University at Urbana, USA
- Dubois F, Jean M, Renouf M, Mozul R, Martin A, Bagneris M (2011) LMG90. In: *CSMA 2011 10e Colloque National en Calcul des Structures*, May 2011. Presqu'île de Giens, Var
- Eberhardt E, Stead D, Coggan JS (2004) Numerical analysis of initiation and progressive failure in natural rock slopes—the 1991 Randa rockslide. *Int J Rock Mech Min Sci* 41:69–87. [https://doi.org/10.1016/S1365-1609\(03\)00076-5](https://doi.org/10.1016/S1365-1609(03)00076-5)
- Gong W, Juang CH, Wasowski J (2021) Geohazards and human settlements: lessons learned from multiple relocation events in Badong, China—engineering geologist's perspective. *Eng Geol* 285:106051. <https://doi.org/10.1016/j.enggeo.2021.106051>
- Görüm T (2019) Landslide recognition and mapping in a mixed forest environment from airborne LiDAR data. *Eng Geol* 258:105155. <https://doi.org/10.1016/j.enggeo.2019.105155>
- Griffiths DV, Lane PA (1999) Slope stability analysis by finite elements. *Geotechnique* 49(3):387–403. <https://doi.org/10.1680/geot.1999.49.3.387>
- Gupta V, Jamir I, Kumar V, Devi M (2017) Geomechanical characterisation of slopes for assessing rockfall hazards in the Upper Yamuna Valley, Northwest Higher Himalaya, India. *Himalayan Geol* 38(2):156–170
- Haberman DL, Haberman D (2006) *River of Love in an Age of Pollution*. In: *River of love in an age of pollution*. University of California Press, USA
- Healy D, Rizzo RE, Cornwell DG, Farrell NJ, Watkins H, Timms NE, Gomez-Rivas E, Smith M (2017) FracPaQ: a MATLAB™ toolbox for the quantification of fracture patterns. *J Struct Geol* 95:1–6. <https://doi.org/10.1016/j.jsg.2016.12.003>
- Hoek E, Bray JD (1981) *Rock slope engineering*. CRC Press, USA
- Hoek E, Brown ET (1997) Practical estimates of rock mass strength. *Int J Rock Mech Min Sci* 34(8):1165–1186. [https://doi.org/10.1016/S1365-1609\(97\)80069-X](https://doi.org/10.1016/S1365-1609(97)80069-X)

- Hoek E, Diederichs MS (2006) Empirical estimation of rock mass modulus. *Int J Rock Mech Min Sci* 43(2):203–15
- Hoek E, Kaiser PK, Bawden WF (1995) Support of underground excavations in hard rock. AA Alkema, Rotterdam
- IANS (2018) <https://timesofindia.indiatimes.com/city/dehradun/yamunotri-nh-blocked-after-landslides-at-ojari-dabarkot/articleshow/64952115.cms>
- IANS (2019a) https://www.business-standard.com/article/current-affairs/over-1-lakh-pilgrims-register-for-char-dham-yatra-in-uttarakhand-122042201443_1.html
- IANS (2019b). <https://timesofindia.indiatimes.com/city/dehradun/no-permanent-solution-for-landslide-woes-at-ojari-dabarkot-yet/articleshow/70352032.cms>
- Iverson RM (2000) Landslide triggering by rain infiltration. *Water Resour Res* 36(7):1897–1910. <https://doi.org/10.1029/2000WR900090>
- Jacob J, Sliniski K (2021) FLDAS noah land surface model L4 central Asia daily 0.01×0.01 degree. Goddard Earth Sci Data Inf Serv Cent (GES DISC). <https://doi.org/10.5067/VQ4CD3Y9YC0R>
- Jamir I, Gupta V, Kumar V, Thong GT (2017) Evaluation of potential surface instability using finite element method in Kharsali Village, Yamuna Valley, Northwest Himalaya. *J Mt Sci* 14:1666–1676. <https://doi.org/10.1007/s11629-017-4410-3>
- Jamir I, Gupta V, Thong GT, Kumar V (2020) Litho-tectonic and precipitation implications on landslides, Yamuna valley, NW Himalaya. *Phys Geogr* 41(4):365–388. <https://doi.org/10.1080/02723646.2019.1672024>
- Jang HS, Kang SS, Jang BA (2014) Determination of joint roughness coefficients using roughness parameters. *Rock Mech Rock Eng* 47(6):2061–2073
- Jing L (2003) A review of techniques, advances and outstanding issues in numerical modelling for rock mechanics and rock engineering. *Int J Rock Mech Min Sci* 40(3):283–353. [https://doi.org/10.1016/S1365-1609\(03\)00013-3](https://doi.org/10.1016/S1365-1609(03)00013-3)
- Karar A (2010) Impact of pilgrim tourism at Haridwar. *The Anthropologist* 12(2):99–105. <https://doi.org/10.1080/09720073.2010.11891138>
- Keefer DK (1984) Landslides caused by earthquakes. *Geol Soc Am Bull* 95(4):406–421. [https://doi.org/10.1130/0016-7606\(1984\)95<406:LCBE>2.0.CO;2](https://doi.org/10.1130/0016-7606(1984)95<406:LCBE>2.0.CO;2)
- Korup O (2004) Geomorphic implications of fault zone weakening: slope instability along the Alpine Fault, South Westland to Fiordland. *NZ J Geol Geophys* 47(2):257–267. <https://doi.org/10.1080/00288306.2004.9515052>
- Krautblatter M, Moser M (2009) A nonlinear model coupling rockfall and rainfall intensity based on a four-year measurement in a high Alpine rock wall (Reintal, German Alps). *Nat Hazard* 9(4):1425–1432
- Kumar V, Gupta V, Jamir I, Chatteraj SL (2019) Evaluation of potential landslide damming: case study of Urni landslide, Kinnaur, Satluj valley, India. *Geosci Front* 10(2):753–767
- Kumar V, Cauchie L, Mreyen AS, Micu M, Havenith HB (2021a) Evaluating landslide response in a seismic and rainfall regime: a case study from the SE Carpathians, Romania. *Nat Hazard* 21(12):3767–3788. <https://doi.org/10.5194/nhess-21-3767-2021>
- Kumar V, Jamir I, Gupta V, Bhasin RK (2021b) Inferring potential landslide damming using slope stability, geomorphic constraints, and run-out analysis: a case study from the NW Himalaya. *Earth Surf Dyn* 9(2):351–377. <https://doi.org/10.5194/esurf-9-351-2021>
- Leine RI, Schweizer A, Christen M, Glover J, Bartelt P, Gerber W (2014) Simulation of rockfall trajectories with consideration of rock shape. *Multibody Syst Dyn* 32(2):241–271
- Leroueil S, Locat J, Vaunat J, Picarelli L, Lee H, Faure R (1996) Geotechnical characterization of slope movements. In: *Landslides*. pp. 53–74
- Li C, Ma T, Zhu X, Li W (2011) The power-law relationship between landslide occurrence and rainfall level. *Geomorphology* 130(3–4):221–229. <https://doi.org/10.1016/j.geomorph.2011.03.018>
- Mărgărint MC, Grozavu A, Patriche CV (2013) Assessing the spatial variability of coefficients of landslide predictors in different regions of Romania using logistic regression. *Nat Hazard* 13(12):3339–3355
- Mauldon M, Dunne WM, Rohrbaugh MB Jr (2001) Circular scanlines and circular windows: new tools for characterizing the geometry of fracture traces. *J Struct Geol* 23(2–3):247–258. [https://doi.org/10.1016/S0191-8141\(00\)00094-8](https://doi.org/10.1016/S0191-8141(00)00094-8)
- McNally A, Arsenault K, Kumar S, Shukla S, Peterson P, Wang S, Funk C, Peters-Lidard CD, Verdin JP (2017) A land data assimilation system for sub-Saharan Africa food and water security applications. *Sci Data* 4(1):1–19
- Melillo M, Gariano SL, Peruccacci S, Sarro R, Mateos RM, Brunetti MT (2020) Rainfall and rockfalls in the Canary Islands: assessing a seasonal link. *Nat Hazard* 20(8):2307–2317
- Mohr O (1914) *Treatises from the field of technical mechanics*. W. Ernst & Son
- Morelli S, Monroy VH, Gigli G, Falorni G, Rocha EA, Casagli N (2010) The Tancitaro debris avalanche: characterization, propagation and modeling. *J Volcanol Geoth Res* 193(1–2):93–105. <https://doi.org/10.1016/j.jvolgeores.2010.03.008>
- Ojha AK, Srivastava DC, Sharma R (2022) Fluctuation in the fluid and tectonic pressures in the South Almora Thrust Zone (SATZ), Kumaun Lesser Himalaya; paleoseismic implications. *J Struct Geol* 160:104631. <https://doi.org/10.1016/j.jsg.2022.104631>
- Pradhan RM, Singh A, Ojha AK, Biswal TK (2022) Structural controls on bedrock weathering in crystalline basement terranes and its implications on groundwater resources. *Sci Rep* 12(1):11815. <https://doi.org/10.1038/s41598-022-15889-x>
- Qi T, Meng X, Qing F, Zhao Y, Shi W, Chen G, Zhang Y, Li Y, Yue D, Su X, Guo F (2021) Distribution and characteristics of large landslides in a fault zone: a case study of the NE Qinghai-Tibet Plateau. *Geomorphology* 379:107592. <https://doi.org/10.1016/j.geomorph.2021.107592>
- Roy P, Jain N, Martha TR, Kumar KV (2022) Reactivating Balia Nala landslide, Nainital, India—a disaster in waiting. *Landslides*. <https://doi.org/10.1007/s10346-022-01881-z>
- Scheingross JS, Minchew BM, Mackey BH, Simons M, Lamb MP, Hensley S (2013) Fault-zone controls on the spatial distribution of slow-moving landslides. *Bulletin* 125(3–4):473–489. <https://doi.org/10.1130/B30719.1>
- Searle MP, Metcalfe RP, Rex AJ, Norry MJ (1993) Field relations, petrogenesis and emplacement of the Bhagirathi leucogranite, Garhwal Himalaya. *Geol Soc* 74(1):429–444. <https://doi.org/10.1144/GSL.SP.1993.074.01.29>
- Setiawan H, Wilopo W, Wiyoso T, Fathani TF, Karnawati D (2019) Investigation and numerical simulation of the 22 February 2018 landslide-triggered long-traveling debris flow at Pasir Panjang Village, Brebes Regency of Central Java, Indonesia. *Landslides* 16(11):2219–2232. <https://doi.org/10.1007/s10346-019-01245-0>
- Shaller PJ, Doroudian M, Hart MW, Chen MT (2020) The Eureka Valley landslide: evidence of a dual failure mechanism for a long-runout landslide. *Lithosphere* 2020(1) <https://doi.org/10.2113/2020/8860819>
- Singh K, Thakur VC (2001) Microstructures and strain variation across the footwall of the Main Central Thrust Zone, Garhwal Himalaya, India. *J Asian Earth Sci* 19(1–2):17–29. [https://doi.org/10.1016/S1367-9120\(00\)00006-7](https://doi.org/10.1016/S1367-9120(00)00006-7)
- Srivastava HB, Tripathy NR (2007) Geometrical analysis of mesoscopic shear zones in the crystalline rocks of MCT Zone of

- Garhwal Higher Himalaya. *J Asian Earth Sci* 30(5–6):599–612. <https://doi.org/10.1016/j.jseae.2006.10.003>
- Stanley T, Kirschbaum DB, Pascale S, Kapnick S (2020) Extreme precipitation in the Himalayan landslide hotspot. Satellite precipitation measurement. Springer, Cham, pp 1087–1111
- Sundriyal Y, Kumar V, Chauhan N, Kaushik S, Ranjan R, Punia MK (2023a) Brief communication: the Northwest Himalaya towns slipping towards potential disaster. *Nat Hazard* 23(4):1425–1431
- Sundriyal Y, Kumar V, Khan F, Puniya MK, Kaushik S, Chauhan N, Bagri DS, Rana N (2023b) Impact of potential flood on riverbanks in extreme hydro-climatic events, NW Himalaya. *Bull Eng Geol Environ* 82:196
- Take WA, Beddoe RA, Davoodi-Bilesavar R, Phillips R (2015) Effect of antecedent groundwater conditions on the triggering of static liquefaction landslides. *Landslides* 12(3):469–479. <https://doi.org/10.1007/s10346-014-0496-7>
- Terzaghi K (1950) Mechanism of landslides. In: Application of geology to engineering practice. Sidney Paige. <https://doi.org/10.1130/Berkey.1950.83>
- Upton P, Song BR, Koons PO (2018) Topographic control on shallow fault structure and strain partitioning near Whataroa, New Zealand demonstrates weak Alpine Fault. *NZ J Geol Geophys* 61(1):1–8. <https://doi.org/10.1080/00288306.2017.1397706>
- Varnes DJ (1978) Slope movement types and processes. *Special Rep* 176:11–33
- Wang F, Fan X, Yunus AP, Siva Subramanian S, Alonso-Rodriguez A, Dai L, Xu Q, Huang R (2019) Coseismic landslides triggered by the 2018 Hokkaido, Japan (Mw 6.6), earthquake: spatial distribution, controlling factors, and possible failure mechanism. *Landslides* 16(8):1551–66. <https://doi.org/10.1007/s10346-019-01187-7>
- Wei J, Zhao Z, Xu C, Wen Q (2019) Numerical investigation of landslide kinetics for the recent Mabian landslide (Sichuan, China). *Landslides* 16(11):2287–2298. <https://doi.org/10.1007/s10346-019-01237-0>
- Zheng H, Shi Z, Shen D, Peng M, Hanley KJ, Ma C, Zhang L (2021) Recent advances in stability and failure mechanisms of landslide dams. *Front Earth Sci* 9:201. <https://doi.org/10.3389/feart.2021.659935>

Publisher's Note Springer Nature remains neutral with regard to jurisdictional claims in published maps and institutional affiliations.

Springer Nature or its licensor (e.g. a society or other partner) holds exclusive rights to this article under a publishing agreement with the author(s) or other rightsholder(s); author self-archiving of the accepted manuscript version of this article is solely governed by the terms of such publishing agreement and applicable law.